Micrometeorite Impact Annealing of Ice in the Outer Solar System

Simon B. Porter[a], Steven J. Desch[a], and Jason C. Cook[b]

[a]*School of Earth and Space Exploration, Arizona State University, Tempe, AZ 85287 (U.S.A.)*

[b]*Southwest Research Institute, 1050 Walnut Street, Boulder, CO 80302*

Abstract

The spectra of water ice on the surfaces of icy satellites and Kuiper Belt Objects (KBOs) indicate that the surface ice on these bodies is in a crystalline state. This conflicts with theoretical models, which predict that radiation (Galactic cosmic rays and solar ultraviolet) should damage the crystalline structure of ice on geologically short timescales. Temperatures are too low in the outer solar system for the ice to anneal, and reflectance spectra of these bodies should match those of amorphous solid water (ASW). We assess whether the kinetic energy deposited as heat by micrometeorite impacts on outer solar system bodies is sufficient to anneal their surface ice down to a near infrared optical depth (350 μm). We calculate the kinetic energy flux from interplanetary micrometeorite impacts, including gravitational focusing. We also calculate the thermal diffusion of impact heat in various surfaces and the rate of annealing of ice. We conclude that the rate of annealing from micrometeorite impacts is sufficient to explain the crystallinity of ice on nearly all the surfaces of the saturnian, uranian and neptunian satellites. We discuss how the model can be used in conjunction with spectra of KBOs to probe dust fluxes in the Kuiper Belt.

Key words: SATELLITES, SURFACES, ICES, IR SPECTROSCOPY, SATURN, SATELLITES, URANUS, SATELLITES, KUIPER BELT, INTERPLANETARY DUST

1 Introduction

Effectively airless icy objects in the outer solar system — satellites, comets, and Kuiper Belt Objects (KBOs) — play host to one of the most common but least understood solid surfaces in the solar system. While spacecraft have

observed their large-scale morphologies, which often are dominated by impact craters and tectonic features, the nature of their surfaces remain difficult to observe at small scales. Reflectance spectra represent the most reliable way of probing the composition of their surfaces. The dominant features in the reflectance spectra of outer solar system bodies are the vibrational modes of water ice, in the infrared. More detailed modeling often reveals that their surfaces are porous regoliths of mainly water ice, mixed with various organics, and a spectrally neutral phase, possibly hydrated silicates (Roush, 2001).

At low pressures below 150 K, water ice can exist in either a crystalline state (either hexagonal Ih or cubic Ic ice) or as amorphous ice (amorphous solid water; ASW) (Jenniskens and Blake, 1996). These can be spectrally distinguished by an absorption feature at 1.65 μm, which is strong in both Ic and Ih (especially at low temperatures: Mastrapa and Brown (2006)), but is much weaker in ASW. Spectra returned by the Visual and Infrared Mapping Spectrometer (VIMS) on the NASA/ESA *Cassini* spacecraft appear to show that crystalline water is present on the surfaces of nearly all the airless satellites of Saturn (Filacchione et al., 2007). In addition, ground-based spectra of both the regular satellites of Uranus (Bauer et al., 2002; Grundy et al., 2006) and several Kuiper Belt Objects (KBOs) also appear to show the 1.65 μm feature (Barkume et al., 2008; Cook et al., 2007; Jewitt and Luu, 2004). Nearly every large (¿200 km) outer solar system body with water ice has shown evidence of crystalline water ice.

The prevalence of crystalline water ice surfaces beyond Jupiter's orbit is unexpected (Jenniskens and Blake, 1996). Below approximately 150 K, water vapor will deposit onto a surface as ASW, and can only be annealed to crystalline ice through the application of external heat (Jenniskens and Blake, 1996). More important, the crystalline structure of ice can be damaged by radiation; laboratory tests have shown that both solar ultraviolet (UV) radiation (Leto and Baratta, 2003) and Galactic cosmic rays (Mastrapa and Brown, 2006) can convert crystalline ice into ASW. The timescales for this amorphization are on the order of 1500 kyr for Galactic cosmic rays (GCRs) throughout the outer solar system, and 50 kyr for UV amorphization at 40 AU (assuming that all solar UV photons shortward of 200 nm are as capable, per photon energy, at amorphizing ice as Lyα photons), decreasing with greater distance from the Sun (Cook et al., 2007). Some widespread annealing process must therefore be effectively competing with GCRs and solar UV in order for the 1.65 μm spectral feature to be so common.

Cook et al. (2007) reviewed several annealing mechanisms in the context of Charon, all of which are applicable to icy objects in general. A solid-state greenhouse effect, utilizing ice's transparency in the visual and opacity in the infrared, was shown to be ineffective at raising the temperature of surface ice more than a few Kelvin on that body. Likewise, solid-state convection cannot

work effectively to expose subsurface crystalline ice for surface temperatures below 140 K (at which point ASW would self-anneal), because the viscosity is too high. Cook et al. (2007) therefore favored for Charon the mechanism of cryovolcanism, in which subsurface liquid water erupts on the surface, freezing on the surface at above 150 K, and preserving its crystalline structure as it cools to the ambient temperature. Radar mapping by *Cassini* appears to show several surface morphologies on Titan that could indicate cryovolcanic flows (Lopes et al., 2007). In addition, imaging by NASA's *Voyager 2* spacecraft appeared to show cryovolcanic flow features on both Ariel (Smith et al., 1986) and Triton (Smith et al., 1989). Desch et al. (2009) have recently shown through thermal interior modeling that cryovolcanism may be presently acting on many KBOs or icy satellites at least 600 km in radius and contain ammonia. However, many icy satellites with crystalline ice features are simply too small to sustain cryovolcanism, and an alternative annealing mechanism is still sought.

One final method reviewed by Cook et al. (2007) was micrometeorite impact annealing. In this process, interplanetary dust particles (IDPs) impact the surface ice and deposit their kinetic energy as heat. This heat then diffuses into the surrounding ice, briefly raising its temperature high enough to cause the ice to crystallize (into either Ic or Ih). Cook et al. (2007) did not favor this mechanism for KBOs or Charon, because the dust fluxes were thought to be too low (we revisit this point below). However, because IDPs are gravitationally focused in the gravity wells of large planets (Krivov et al., 2003), the IDP kinetic energy fluxes at the orbits of the saturnian and uranian regular satellites can be much enhanced over the values previously inferred by Cook et al. (2007) for KBOs.

This paper re-examines the role of micrometeorite annealing on the crystallinity of ice on outer solar system icy bodies. First, the impact annealing process will be described and quantified. Next, it will be applied to the icy satellites of Saturn, Uranus, and Neptune. Finally, micrometeorite annealing on KBOs will estimated, and methods of using micrometeorite annealing as a probe of Kuiper Belt dust production will be discussed.

2   Modeling Micrometeorite Annealing

In order to quantify the rate at which kinetic energy deposited by micrometeorite impacts could anneal ice on a surface, we first simulated the effects of a single impact. Cook et al. (2007) laid the groundwork for this model by estimating the mass of surface ice raised to greater than 185 K (even if only for a fraction of a second) during a given impact event. Under conditions appropriate for Charon, they found that ice approximately ten times the mass of the

impactor is annealed. However, the micrometeorites impacting the moons of Saturn and Uranus are considerably faster and of higher number density than in the Kuiper Belt, due chiefly to planetary gravity (see below). We therefore decided to attempt a more rigorous simulation of the annealing of these moons' surface ice.

2.1 Theoretical Model

For the model, we assumed the micrometeorites implant themselves deeply (many particle diameters) in the icy regolith, and deposit a fraction ξ of their kinetic energy as heat where they are stopped. Typically $\xi = 2/3$, the rest being converted into mechanical work (Hartmann, 1985). This heat then diffuses spherically outward through the ice, assumed to be ASW. It is assumed in the calculations that the micrometeorites stop at depths at least 30 times their own radius, justifying spherical symmetry. Laboratory tests of hypervelocity impacts into silicate regoliths actually indicate that impactors generally do not penetrate that deep (Hartmann, 1985), so that some fraction of heat energy necessarily is lost at the surface and does not anneal ice, effectively lowering ξ.

While most of the mid-size moons of Saturn have a nearly pure ice surface (Grundy et al., 1999), the surfaces of the moons of Uranus as well as nearly every KBO have mixtures of organics and silicates with a lower thermal conductivity than ice (Barkume et al., 2008; Grundy et al., 2006), which will lead to a higher fraction of ice being annealed than this model estimates.

In the results described below, we sought to parameterize these limits to the amount of ASW that a single impact can convert to crystalline ice. For the thermal model, we therefore set $\xi = 1$, allowing a lower ξ to be used once the relationship between energy and mass annealed is known (see Equation 6).

Within the model, the ice to be annealed is broken into 300 spherical shells of equal thickness Δx. The simulation is initialized by depositing the kinetic energy of the impactor evenly in the 10 innermost zones. All other zones are initialized at the given surface temperature. To convert between temperature and energy, we assumed the following simplified Debye model for specific heat within shell i (bounded by radii x_{i-1} and x_i):

$$E_i(T) = \int_0^T M_i\, C_P(T')\, dT' \approx \rho\, A\, T^2, \tag{1}$$

where M_i is the mass within shell i, equal to its volume times the material density ρ: $M_i = (4\pi/3)\left(x_i^3 - x_{i-1}^3\right)\rho$. For the innermost 10 zones correspond-

ing to the impactor, we have assumed parameters appropriate for a silicate IDP (Messenger et al., 2003), $A = 1.4 \, \mathrm{J \, kg^{-1} \, K^{-2}}$ [corresponding to a heat capacity of $280 \, (T/100 \, \mathrm{K}) \, \mathrm{J \, kg^{-1} \, K^{-1}}$], and $\rho = 2500 \, \mathrm{kg \, m^{-3}}$. For the surrounding ice, we have assumed $A = 3.87 \, \mathrm{J \, kg^{-1} \, K^{-2}}$ [corresponding to a heat capacity of $773 \, (T/100 \, \mathrm{K}) \, \mathrm{J \, kg^{-1} \, K^{-1}}$], and $\rho = 500 \, \mathrm{kg \, m^{-3}}$, which implies a regolith porosity of 0.5 (Grundy et al., 1999). We then calculated the spherically symmetric heat flux (evaluated at the boundaries of zones) to be

$$F_i \equiv \mathrm{Flux}(i \to i+1) = -k \left. \frac{\partial T}{\partial r} \right|_{x_i} = -\frac{(k_i + k_{i+1})}{2} \cdot \frac{T_{i+1} - T_i}{(x_{i+1} - x_{i-1})/2}, \quad (2)$$

and the resulting change in internal energy in zone i over a timestep Δt to be

$$\Delta E_i = \left(4\pi x_{i-1}^2 F_{i-1} - 4\pi x_i^2 F_i \right) \Delta t, \quad (3)$$

where k_i, and T_i are the thermal conductivity and temperature within shell i, evaluated at its center. We approximated the conductivity of the regolith to be that of crystalline ice (Klinger, 1980), setting $\rho = 0.5$ to account for porosity:

$$k(T) = 567 \left(\frac{\rho}{1 \, \mathrm{g \, cm^{-3}}} \right) \left(\frac{T}{K} \right)^{-1} \mathrm{W \, m^{-1} \, K^{-1}} \quad (4)$$

The thermal conductivity of crystalline ice is much higher than ASW (Andersson and Suga, 2002), and thus a provides a lower limit on the mass annealed. Once the new thermal energies of all shells are calculated, Equation 1 is then inverted to find the new temperatures within the shells at each timestep.

The temperature within a shell, and the length of time it spends at each temperature, are used to assess whether the ice in the shell is annealed. Based on the data in Baragiola (2003), we assumed that the time it takes to fully anneal a sample of amorphous solid water is

$$t_{\mathrm{anneal}} \approx 8 \times 10^{16} \exp \left(-\frac{0.225 \, \mathrm{T}}{K} \right) \mathrm{s} \quad (5)$$

During each timestep of length Δt (10^{-6} s), we assume a fraction $\Delta t / t_{\mathrm{anneal}} \ll 1$ of the ice is annealed.

5

We implemented the model above using a computer program in the C++ language with inputs of surface ice temperature T_{surf}, impactor diameter D_{p}, and impactor velocity V_{imp}, and outputs of mass annealed M_{anneal} and effective diffusion time. We then ran this program across a parameter space ranging from $T_{\mathrm{surf}} = 40 - 100\,\mathrm{K}$, $D_{\mathrm{p}} = 10 - 150\,\mu\mathrm{m}$, and $V_{\mathrm{imp}} = 1 - 25\,\mathrm{km\,s^{-1}}$, at increments of $10\,\mathrm{K}$, $10\,\mu\mathrm{m}$, and $1\,\mathrm{km\,s^{-1}}$. Because the computing time needed to conduct a single impact simulation is long, we decided to seek an emperical relationship between the inputs and the mass of ice annealed per impact. We plotted the total mass annealed per impact versus the impactor's kinetic energy, and results can be seen in Figure 1. Because the diffusion times were so fast (less than a minute in all but highest energy cases), the mass annealed was mostly insensitive to the surface ice temperature. In addition, only the inner few shells were generally vaporized, and quickly recondensed, thus confirming the calculation of Cook et al. (2007). There did appear to be a strong power-law correspondence between the mass annealed and the impact energy. Using a simple regression fit, we found this relationship to be

$$M_{\mathrm{anneal}} \approx 3.9 \times 10^{-7} \left(\xi \, \frac{KE}{1\,\mathrm{J}} \right)^{1.33} \mathrm{kg} \tag{6}$$

Where KE is the impactor's kinetic energy, and ξ is the efficiency factor in converting KE into thermal energy capable of annealing ice, $\approx 2/3$ (Hartmann, 1985). Equation 6 also shows that the mass annealed, and thus the annealing rate, is directly proportional to $\xi^{1.33}$. The scatter in the plot is mainly due to there being a larger amount of data points with a moderate kinetic energy (e.g. large and slow or small and fast IDP) than the upper and lower ends of the energy range.

In order to estimate the effect of a rockier regolith, we ran a modified version of the above model with a 50% rock, 50% ice composition, with the thermal conductivities blended in the same way as in Desch et al. (2009). The result was that slightly more than half the mass of ice was annealed for a given input energy and regolith volume, resulting in relative crystalline fractions 10-20% higher than for pure ice. The fraction of ice annealed is mostly a function of the time the ice spends above the annealing point, rather than the peak temperature. Thus, the slower thermal conductivity of the rock in the regolith allows for longer diffusion times, and thus slightly more annealing. Amorphous ice also has a lower thermal conductivity than crystalline ice, and versions of the code that accounted for this showed a similar effect. We thus considered the canonical case (all crystalline conductivity) to be a lower limit to ice annealed per impact.

Finally, we constructed a third model to represent the case where the micrometeorite distributes its energy equally along a linear path down to 350 μm, the optical depth of ice for 1.6 μm near infrared (NIR). Since there is no energy difference along the path, and thus no vertical thermal diffusion, this can be modeled as a one-dimensional cylindrical geometry, with heat diffusing perpendicular to the path. Since the major bottleneck to annealing in the spherical case was in transporting the heat initially out of the micrometeorite, the larger initial heated volume of the linear case promised a higher annealed mass. This did indeed turn out to be the case for most impact energies, with the linear pure ice model annealing up to a factor of ten more ice than the spherical pure ice model (Eq. 6). On the other hand, micrometeorites at the smaller / slower end of the considered range tended to dump their energy into the ice too fast, annealing as little as a quarter of the ice annealed in the spherical case. Since the actual diffusion geometry in real impacts would be somewhere in between these two end members, we considered the model fit to the spherical case to be a realistic conservative estimate.

3   Annealing on Icy Satellites

Observing the surfaces of airless icy satellites is on the one hand eased by the lack of any substantial interference other than telluric, but is also complicated by their small angular size. Grundy et al. (1999) provide a very comprehensive collection of near-infrared ground-based spectra for large icy satellites. Europa and Ganymede both show noticeable 1.65 μm features, while the rockiness of Callisto mostly obscures the vibrational modes of water. Likewise, Iapetus, Rhea, Dione, Tethys, Enceladus, and the A and B rings all show deep absorption features at 1.65 μm. This has been confirmed by measurements from *Cassini* (Filacchione et al., 2007), and crystallinity maps are available for Enceladus (Newman et al., 2008). Ground-based spectra also show crystalline ice on all of the five regular satellites of Uranus, though the signal-to-noise for Umbriel is low due to the small amount of exposed ice on its surface (Bauer et al., 2002; Grundy et al., 1999, 2006).

3.1   Dust Sources

Micrometeorites that impact icy satellites can have two sources: interplanetary dust swept up by the planet's gravity; and dust particles native to the planetary system. Dust in orbit around the planet naturally imparts less kinetic energy onto satellites, due to its lower velocity relative to the satellites; it is therefore only competitive with IDPs at very high densities, such as in a planetary ring. The only dense ring known to hold large satellites is the E-

ring of Saturn. Measurements of dust flux by the *Cassini* spacecraft appear to show that Enceladus is the source of the E-ring dust (Spahn et al., 2006). As can be seen in Figure 2, only at Enceladus is the E-ring dense enough to have a kinetic energy flux comparable to (though lower than) IDPs at the same radius. The primary dust source for micrometeorite annealing on icy satellites is therefore interplanetary dust particles.

Dust densities are difficult to measure obsevationally, and so spacecraft mission offer the best dust data for the outer solar system. The first in-situ measurements of IDPs beyond the orbit of Jupiter were made by NASA's *Pioneer 10* and *11* spacecraft in the 1970s (Humes, 1980). Though the *Pioneer 11* detector was saturated during its close encounter with Saturn, the *Pioneer 10* detector reported the interplanetary dust flux out to 18 AU. It found that the spatial density of particles $\geq 10^{-12}$ kg was nearly constant from Jupiter out to 18 AU, implying that Uranus encounters a similar flux as Saturn. Divine (1993) modeled this data and Krivov et al. (2003) adapted it to find a dust flux of 1.8×10^{-16} kg m^{-2} s^{-1} at Saturn; applying their modeling we expect a flux at Uranus of 1.2×10^{-16} kg m^{-2} s^{-1}. Further modeling by Liou and Zook (1999) has revealed the two-dimensional structure of Kuiper Belt dust, and implies that the dust spatial density is similar at Neptune to Uranus (see their Figure 7). Scaling for orbital velocity, we can then assume the IDP flux at Neptune to be approximately 1.0×10^{-16} kg m^{-2} s^{-1}. Experimental confirmation of these fluxes is being collected now by the Student Dust Counter on NASA's *New Horizons* spacecraft, which passed the orbit of Saturn in June 2008 and will reach Pluto in July 2015 (Horányi et al., 2008). The Student Dust Counter has a sensitivity down to 10^{-15} kg, and so could detect whole populations of IDPs missed by *Pioneer 10*.

3.2   Gravitational Focusing

To find the amount of ice that could be annealed by IDPs, we need to find the kinetic energy they deposit on the satellites' surfaces. As an IDP enters a planet's Hill radius, it is accelerated towards the planet. Thus, both the velocity and the number of IDPs increases dramatically close to the planet. Colombo et al. (1966) found (using energy conservation arguments) the velocity scaling as a dust particle approaches a planet to be the sum in quadrature of the IDP's heliocentric velocity and the planetocentric escape velocity:

$$\frac{v_{\mathrm{imp}}}{v_{\mathrm{imp}}^{\infty}} = \sqrt{1 + \frac{2GM_{\mathrm{p}}}{r(v_{\mathrm{imp}}^{\infty})^2}}, \qquad (7)$$

where M_{p} is the planet's mass, r the distance from the planet, and v_{imp}^{∞} is the dust's distant velocity relative to the planet, assumed here to be the planet's

orbital velocity times $\sqrt{e^2 + i^2}$, where $e \approx i \approx 0.3$. Spahn et al. (2006) corrected Colombo et al. (1966) to find the number density scaling to be

$$\frac{n_{\text{imp}}}{n_{\text{imp}}^\infty} = \frac{1}{2}\frac{v_{\text{imp}}}{v_{\text{imp}}^\infty} + \frac{1}{2}\left[\left(\frac{v_{\text{imp}}}{v_{\text{imp}}^\infty}\right)^2 - \left(\frac{R_\text{p}}{r}\right)^2\left(1 + \frac{2GM_\text{p}}{R_\text{p}(v_{\text{imp}}^\infty)^2}\right)\right]^{1/2}. \tag{8}$$

The velocity with which an IDP impacts a satellite is a combination of both its velocity relative to the planet, as well as the satellite's planetocentric velocity, V_{sat}. If we assume that a median impact is perpendicular to the satellite's orbit, we can find the average kinetic energy on impact, $KE_{\text{imp}} = (1/2)m_{\text{imp}}V_{\text{net}}^2$, where the impact velocity is

$$V_{\text{net}} = \sqrt{V_{\text{sat}}^2 + \left(\frac{V_{\text{imp}}}{V_{\text{imp}}^\infty}V_{\text{imp}}^\infty\right)^2}. \tag{9}$$

To account for the eccentricity of satellites' orbits, the kinetic energy flux was numerically integrated and averaged over a full orbit. Since nearly all these satellites have circular orbits, this was generally a negligible effect, although the annealing rate on the highly eccentric satellite Nereid was doubled compared to the case where its orbit had zero eccentricity. Knowing the average kinetic energy imparted per impact, Equation 6 was used to find the mean mass of ice annealed per micrometeorite impact, $\bar{m}_{\text{anneal}}$.

The annealing rate was then found by multiplying the mass annealed per impact by the number of impacts with this energy. This is related to the flux of kinetic energy onto the satellites,

$$KE_{\text{flux}} = \left(\frac{F_{\text{imp}}^\infty}{v_{\text{imp}}^\infty}\right)\left(\frac{n_{\text{imp}}}{n_{\text{imp}}^\infty}\right)\frac{V_{\text{net}}^3}{2} \tag{10}$$

where F_{imp}^∞ is the distant mass flux of IDPs in $\text{kg}\,\text{m}^{-2}\,\text{s}^{-1}$. The rate at which ice is annealed on the surface of a satellite (mass per area per time) is then straightforwardly found to be $(KE_{\text{flux}}/KE_{\text{imp}})\,\bar{m}_{\text{anneal}}$, and the timescale to anneal all but $1/e$ of the ice down to a depth d_{ice} is

$$\tau_{\text{anneal}} \approx 0.63\, d_{\text{ice}}\rho_{\text{ice}}\,\frac{KE_{\text{imp}}}{KE_{\text{flux}}\,\bar{m}_{\text{anneal}}}. \tag{11}$$

3.3 Ice Amorphization

The most effective process micrometeorite annealing has to compete with is the conversion of crystalline water ice into amorphous solid water by either

9

ultraviolet or GCR ion irradiation. Leto and Baratta (2003) have shown that low-temperature (16 K) ice exposed to Lyman α radiation will have its spectral signature transformed from crystalline (strong 1.65 μm feature) to amorphous (weak 1.65 μm feature) with a dosage of $\approx$ 10 eV/molecule. Likewise, Mastrapa and Brown (2006) have shown that a similar dose of protons is sufficient to amorphize ice at 40 K, but starts to become ineffective above 50 K. Since the H_2O ice temperatures reported by Grundy et al. (1999) for the Saturnian and Uranian systems are all above 70K, the efficiency of radiation amorphization per eV of dose should be considerably lower for icy satellites than in the colder Kuiper Belt. On the other hand, while the GCR dose is smaller closer to the Sun (deeper into the solar magnetosphere), the UV flux is much larger, as it scales with total solar flux. We therefore used a constant amorphization timescale of 1500 kyr for Galactic cosmic rays (GCRs) throughout the outer solar system. Solar wind particle radiation was not considered, as it is sufficiently weak in the outer solar system that GCRs dominate the radiation dose. We also did not consider the effects of sputtering from either GCRs or the IDPs themselves, as the yields are very low compared to the expected annealing and amorphization rates. In addition, sputtered H_2O would probably recondense in the regolith (Hapke, 1986) with sufficient thermal energy to form crystalline ice.

Cook et al. (2007) estimated that the UV amorphization timescale to be $\approx$40 kyr to anneal the fraction $(1 - e^{-1} \approx 63\%)$ of crystalline ice down to 0.35 mm, the $1/e$ optical depth of ice at 1.65 μm. Considering the constraints above, we estimate the lower limit to the UV amorphization time τ_{amor} to be 150 kyr, 100 kyr, and 50 kyr, for the saturnian, uranian, and neptunian systems, respectively. Since both τ_{amor} and τ_{anneal} are timescales to modify $\approx$ 63% of the ice, their relative proportion gives the fraction of ice currently in steady state crystalline form on an icy satellite's surface:

$$\%_{\mathrm{Crystalline}} = \frac{\tau_{amor}}{\tau_{anneal} + \tau_{amor}} \cdot 100\% \qquad (12)$$

It should also be noted that Mastrapa et al. (2008) have shown that only a 20% fraction of crystalline ice is sufficient to make a sample's spectra look nearly fully crystalline. Therefore, a crystalline fraction greater than 20% should be considered sufficient to explain most observed crystalline features.

3.4 Icy Satellite Results

Table 1 lists the results of the above analysis for several icy satellites. In general, micrometeorite impact heating was found to be effective in annealing amorphous solid water into crystalline ice in fractions that can explain

10

observed icy satellite spectra. Specifically, the number density and velocity scaling from gravitational focusing greatly increased the effectiveness of micrometeorites, by up to three orders of magnitude. In addition, the increased dust densities closer to the Sun allowed for generally higher crystalline fractions at Saturn relative to Neptune. This, though, appears to be a second-order effect when compared to gravitational focusing from the planets.

The three icy satellites of Jupiter have surface temperatures that could self-anneal amorphous ice (Grundy et al., 1999), but also inhabit the very high radiation environment of the jovian magnetosphere. Determining the effect, therefore, of micrometeorite impacts on surface crystallinity is difficult; for a full treatment, see Hansen and McCord (2004). Nonetheless, we calculate that the micrometeorite annealing times for Europa, Ganymede, and Callisto to be 2.3 kyr, 6.7 kyr, and 24 kyr, respectively.

The saturnian system boasts a great variety of icy satellites, and their wide range of orbits shows the effectiveness of gravitational focusing. While close-in Mimas is annealed very rapidly (4.4 kyr), distant Phoebe is only annealed in 14 Myr. Enceladus's active endogenic processes (Waite et al., 2006) may mask any effect of IDP micrometeorites, especially in the southern hemisphere. However, on the apparently more geologically quiescent Mimas, Tethys, Dione, Rhea, and Iapetus, micrometeorite annealing may be the dominant active process controlling the observed ice spectra. Hyperion and Phoebe are both irregular, low density objects whose pockmarked surfaces may act as blackbody cavities to mask their thermal infrared spectral structure (Cooper et al., 2002). However, their surface ice could still be noticeably affected by micrometeorite impact heating. Titan was obviously not considered due to its dense atmosphere.

Uranus has five regular satellites orbiting around its askew rotational axis. Though this means that the effective day/night cycle on these moons is 84 years, this is sufficiently lower than the predicted annealing and amorphization timescales as to not be a concern. The regular spacing of their orbits also shows very well the drop-off of gravitational focusing with distance from the host planet. The uranian satellites have considerably more non-icy material on their surfaces than the similar-sized moons of Saturn, but still show strong crystalline ice spectral signatures. This corresponds well with the predicted annealing timescales, which range from 121 kyr for Mimas, to 2.4 Myr for Oberon.

The satellite system of Neptune is less regular. The close-in proximity of Proteus to the planet allows for a comparable annealing rate to Rhea. Triton is probably a captured dwarf planet from the Kuiper Belt (Agnor and Hamilton, 2006), and the active geysers and surface features observed on it by the NASA *Voyager 2* probe may mask any IDP annealing signature. Nereid is notable

11

for its highly eccentric orbit (e=0.75) which nearly doubles its annealing rate, but not enough to effectively anneal its surface.

To see the upper bound of the annealing based on uncertainties in the *Pioneer 10* data, Table 1 lists the effectiveness of multiplying IDP fluxes by ten. This increases the number of satellites on which micrometeorite annealing is effective by one or two per planetary system. Likewise, assuming that UV amorphization is ineffective, and the Galactic Cosmic Ray (GCR) amorphization timescale is ≈ 1.5 Myr, allows all but the most distant satellites to be crystalline.

4 Discussion

In addition to the possible diffusion geometries discussed above, some uncertainty in these estimates comes from the estimate of ξ. This estimate is based on relatively low velocity (<5 km/s) laboratory tests onto silicate (versus icy) powders. Additional experimentation would help to constrain this value for high velocity impacts onto cryogenic ices. Also, better constraints on the interplanetary dust flux beyond Jupiter would be very beneficial to estimating annealing rates. The Student Dust Counter on the *New Horizons* spacecraft will help considerably with this, as will *New Horizon*'s direct observations of Pluto and Charon.

The nature of these calculations also allowed for an estimate of the total mass of IDP material that would accumulate on the surfaces of these satellites. Multiplying the gravitationally-focused mass flux by 4.0 Gyr produced a mass density ranging from 300 kg/m^2 (for Mimas) to 30 kg/m^2 (for Phoebe). If all these particles had a mean density of 2500 kg/m^3 (as assumed above), and were stacked with a 50% porosity, they would be 240 mm and 24 mm deep, respectively. While this is deeper than our assumed penetration depths for IDPs, they are reasonable depths to be fully mixed into the regolith by impact gardening in 4.0 Gyr. In addition, if the IDP are sourced mainly from comets and KBO, they could be mostly water ice themselves.

Observationally testing the effectiveness of micrometeorite annealing from Earth requires a well-constrained comparison. The irregular satellites of Neptune could be used, as they all recieve the same solar and galactic illumination, are small enough that endogenic processes would not affect their spectra, but experience a broad range of gravitationally-focused dust velocities. Proteus and Nereid have very different predicted annealing rates, and thus could represent opposite endmembers of micrometeorite annealing effectiveness. The spectra of Nereid observed by Brown et al. (1999) show water ice, but not at sufficient resolution to measure crystallinity. Likewise, HST NICMOS pho-

tometry of Proteus did not cover the 1.65 μm feature (Dumas et al., 2003). Future near IR obsevations of theses two satellites are thus required to use them as tests of micrometoerite annealing.

Micrometeorite annealing appears to be effective for most icy satellites, raising the question of how much effect this process may have on Kuiper Belt Objects (KBOs). Since the lower temperatures of the Kuiper Belt allow for faster radiation amorphization times, and considering the lack of a giant planet to gravitationally focus IDPs, the immediate answer would seem to be that annealing should be minimal on these objects. However, the Kuiper Belt is potentially the dustiest part of the solar system (Liou and Zook, 1999). Since no in-situ dust data is available yet for beyond the orbit of Uranus, current models for Kuiper Belt dust are based on dust measurements farther in, and inferences about the rate of inward migration. These models tend to show a peak in dust density at around 40-45 AU. If this true, then KBOs passing through this region could be effectively annealed by micrometeorites.

To quantify this effect, Table 2 lists the IDP fluxes required to anneal a variety of Kuiper Belt objects to 20% crystalline. The UV and GCR amorphization timescales used are the same as previously calculated by Cook et al. (2007) for Charon (40 kyr and 1.5 Myr, respectively). The range of these two timescales thus provides a upper and lower limit to the minimum required dust flux for annealing to be effective. Since the regression fit used in Equation 6 is more appropriate for higher thermal and kinetic energies, the full thermal diffusion model was applied to each case. The calculations were made by integrating each object across its orbit to find the mean kinetic energy flux per a constant mass flux. Generally, the KBOs required an order magnitude less dust than Pioneer 10 observed at Uranus (1.0×10^{-16} kg s^{-1}m^{-2}) to compete with UV amorphization, and even less to compete with galactic cosmic rays.

Since not all of these objects appear to have large amounts of water ice on their surfaces, measuring the crystalline/amorphous ratio can difficult. Values that have been reported in the literature thus far include Orcus at 50% crystalline (Barucci et al., 2008), Quaoar at 50% (Jewitt and Luu, 2004), Charon at 90% (Cook et al., 2007), and Haumea (formerly 2003 EL$_{61}$) at 66-80% (Trujillo et al., 2007) or 40-60% (Pinilla-Alonso et al., 2009). Haumea is an interesting case; it has a highly irregular shape, a rapid rotation rate, and a surface that appears to be mostly water ice (Rabinowitz et al., 2006; Lacerda et al., 2008; Trujillo et al., 2007). Impact annealing could be effective on its surface, explaining its crystallinity without need for surface cryovolcanism. Indeed, as Table 2 shows, micrometeorite annealing is potentially a very effective process for crystallizing surface ice across the Kuiper Belt.

In summary, micrometeorite annealing is effective for most icy satellites. The micrometeorite impact heating process was modeled diffusively for an icy re-

golith, allowing for the estimation of mass annealed per impact as a function of impact kinetic energy. In addition, the gravitational focusing of IDPs by giant planets can considerably increase the micrometeorite kinetic energy flux onto the surfaces of their satellites. These can then be combined to calculate the amount of time to anneal the surface of an icy satellite. UV and ion irradiation work to reverse this process, but not effectively so for nearly all the regular saturnian and uranian satellites. This model has the potential to explain some of the crystalline ice present on Kuiper Belt Objects and could be expanded to use the crystalline fraction measured for KBOs as a probe of dust fluxes in the Kuiper Belt.

References

Agnor, C. B., Hamilton, D. P., May 2006. Neptune's capture of its moon Triton in a binary-planet gravitational encounter. Nature 441, 192–194.

Andersson, O., Suga, H., Mar 2002. Thermal conductivity of amorphous ices. Phys. Rev. B 65 (14), 140201.

Baragiola, R. A., Dec. 2003. Water ice on outer solar system surfaces: Basic properties and radiation effects. Planet. Space Sci. 51, 953–961.

Barkume, K. M., Brown, M. E., Schaller, E. L., Jan. 2008. Near-Infrared Spectra of Centaurs and Kuiper Belt Objects. AJ 135, 55–67.

Barucci, M. A., Merlin, F., Guilbert, A., de Bergh, C., Alvarez-Candal, A., Hainaut, O., Doressoundiram, A., Dumas, C., Owen, T., Coradini, A., Feb. 2008. Surface composition and temperature of the TNO Orcus. A&A 479, L13–L16.

Bauer, J. M., Roush, T. L., Geballe, T. R., Meech, K. J., Owen, T. C., Vacca, W. D., Rayner, J. T., Jim, K. T. C., Jul. 2002. The Near Infrared Spectrum of Miranda: Evidence of Crystalline Water Ice. Icarus 158, 178–190.

Brown, R. H., Cruikshank, D. P., Pendleton, Y., Veeder, G. J., Jun. 1999. NOTE: Water Ice on Nereid. Icarus 139, 374–378.

Colombo, G., Lautman, D. A., Shapiro, I. I., Dec. 1966. The Earth's Dust Belt: Fact or Fiction?, 2, Gravitational Focusing and Jacobi Capture. JGR 71, 5705–+.

Cook, J. C., Desch, S. J., Roush, T. L., Trujillo, C. A., Geballe, T. R., Jul. 2007. Near-Infrared Spectroscopy of Charon: Possible Evidence for Cryovolcanism on Kuiper Belt Objects. ApJ 663, 1406–1419.

Cooper, B. L., Salisbury, J. W., Killen, R. M., Potter, A. E., Apr. 2002. Midinfrared spectral features of rocks and their powders. Journal of Geophysical Research (Planets) 107, 5017–+.

Desch, S. J., Cook, J. C., Doggett, T., Porter, S. B., 2009. Thermal evolution of kuiper belt objects, with implications for cryovolcanism. Icarus 202 (2), 694 – 714.
URL http://www.sciencedirect.com/science/article/B6WGF-4VV2NNN-B/2/ce0fc1e19685035

Divine, N., Sep. 1993. Five populations of interplanetary meteoroids. JGR 98, 17029–17048.

Dumas, C., Smith, B. A., Terrile, R. J., Aug. 2003. Hubble Space Telescope NICMOS Multiband Photometry of Proteus and Puck. AJ 126, 1080–1085.

Filacchione, G., Capaccioni, F., McCord, T. B., Coradini, A., Cerroni, P., Bellucci, G., Tosi, F., D'Aversa, E., Formisano, V., Brown, R. H., Baines, K. H., Bibring, J. P., Buratti, B. J., Clark, R. N., Combes, M., Cruikshank, D. P., Drossart, P., Jaumann, R., Langevin, Y., Matson, D. L., Mennella, V., Nelson, R. M., Nicholson, P. D., Sicardy, B., Sotin, C., Hansen, G., Hibbitts, K., Showalter, M., Newman, S., Jan. 2007. Saturn's icy satellites investigated by Cassini-VIMS. I. Full-disk properties: 350-5100 nm reflectance spectra and phase curves. Icarus 186, 259–290.

Grundy, W. M., Buie, M. W., Stansberry, J. A., Spencer, J. R., Schmitt, B., Dec. 1999. Near-Infrared Spectra of Icy Outer Solar System Surfaces: Remote Determination of H_2O Ice Temperatures. Icarus 142, 536–549.

Grundy, W. M., Young, L. A., Spencer, J. R., Johnson, R. E., Young, E. F., Buie, M. W., Oct. 2006. Distributions of H_2O and CO_2 ices on Ariel, Umbriel, Titania, and Oberon from IRTF/SpeX observations. Icarus 184, 543–555.

Hansen, G. B., McCord, T. B., Jan. 2004. Amorphous and crystalline ice on the Galilean satellites: A balance between thermal and radiolytic processes. Journal of Geophysical Research (Planets) 109 (E18), 1012–+.

Hapke, B., May 1986. On the sputter alteration of regoliths of outer solar system bodies. Icarus 66, 270–279.

Hartmann, W. K., Jul. 1985. Impact experiments. I - Ejecta velocity distributions and related results from regolith targets. Icarus 63, 69–98.

Horányi, M., Hoxie, V., James, D., Poppe, A., Bryant, C., Grogan, B., Lamprecht, B., Mack, J., Bagenal, F., Batiste, S., Bunch, N., Chanthawanich, T., Christensen, F., Colgan, M., Dunn, T., Drake, G., Fernandez, A., Finley, T., Holland, G., Jenkins, A., Krauss, C., Krauss, E., Krauss, O., Lankton, M., Mitchell, C., Neeland, M., Reese, T., Rash, K., Tate, G., Vaudrin, C., Westfall, J., Oct. 2008. The Student Dust Counter on the New Horizons Mission. Space Science Reviews 140, 387–402.

Humes, D. H., Nov. 1980. Results of Pioneer 10 and 11 meteoroid experiments - Interplanetary and near-Saturn. JGR 85, 5841–5852.

Jenniskens, P., Blake, D. F., Dec. 1996. Crystallization of Amorphous Water Ice in the Solar System. ApJ 473, 1104.

Jewitt, D. C., Luu, J., Dec. 2004. Crystalline water ice on the Kuiper belt object (50000) Quaoar. Nature 432, 731–733.

Klinger, J., Jul. 1980. Influence of a phase transition of ice on the heat and mass balance of comets. Science 209, 271–+.

Krivov, A. V., Sremcevic, M., Spahn, F., Dikarev, V. V., Kholshevnikov, K. V., 2003. Impact-generated dust clouds around planetary satellites: spherically symmetric case. Planet. Space Sci. 51 (3), 251 – 269.

Lacerda, P., Jewitt, D., Peixinho, N., May 2008. High-Precision Photometry

of Extreme Kbo 2003 EL$_{61}$. AJ 135, 1749–1756.

Leto, G., Baratta, G. A., Jan. 2003. Ly-alpha photon induced amorphization of Ic water ice at 16 Kelvin. Effects and quantitative comparison with ion irradiation. A&A 397, 7–13.

Liou, J.-C., Zook, H. A., Jul. 1999. Signatures of the Giant Planets Imprinted on the Edgeworth-Kuiper Belt Dust Disk. AJ 118, 580–590.

Lopes, R. M. C., Mitchell, K. L., Stofan, E. R., Lunine, J. I., Lorenz, R., Paganelli, F., Kirk, R. L., Wood, C. A., Wall, S. D., Robshaw, L. E., Fortes, A. D., Neish, C. D., Radebaugh, J., Reffet, E., Ostro, S. J., Elachi, C., Allison, M. D., Anderson, Y., Boehmer, R., Boubin, G., Callahan, P., Encrenaz, P., Flamini, E., Francescetti, G., Gim, Y., Hamilton, G., Hensley, S., Janssen, M. A., Johnson, W. T. K., Kelleher, K., Muhleman, D. O., Ori, G., Orosei, R., Picardi, G., Posa, F., Roth, L. E., Seu, R., Shaffer, S., Soderblom, L. A., Stiles, B., Vetrella, S., West, R. D., Wye, L., Zebker, H. A., Feb. 2007. Cryovolcanic features on Titan's surface as revealed by the Cassini Titan Radar Mapper. Icarus 186, 395–412.

Mastrapa, R. M., Bernstein, M. P., Sandford, S. A., Roush, T. L., Cruikshank, D. P., Ore, C. M. D., Sep. 2008. Optical constants of amorphous and crystalline H$_2$O-ice in the near infrared from 1.1 to 2.6 μm. Icarus 197, 307–320.

Mastrapa, R. M. E., Brown, R. H., Jul. 2006. Ion irradiation of crystalline H$_2$O-ice: Effect on the 1.65-μm band. Icarus 183, 207–214.

Messenger, S., Keller, L. P., Stadermann, F. J., Walker, R. M., Zinner, E., Apr. 2003. Samples of Stars Beyond the Solar System: Silicate Grains in Interplanetary Dust. Science 300, 105–108.

Newman, S. F., Buratti, B. J., Brown, R. H., Jaumann, R., Bauer, J., Momary, T., Feb. 2008. Photometric and spectral analysis of the distribution of crystalline and amorphous ices on Enceladus as seen by Cassini. Icarus 193, 397–406.

Pinilla-Alonso, N., Brunetto, R., Licandro, J., Gil-Hutton, R., Roush, T. L., Strazzulla, G., Mar. 2009. The surface of (136108) Haumea (2003 EL61), the largest carbon-depleted object in the trans-Neptunian belt. A&A 496, 547–556.

Rabinowitz, D. L., Barkume, K., Brown, M. E., Roe, H., Schwartz, M., Tourtellotte, S., Trujillo, C., Mar. 2006. Photometric Observations Constraining the Size, Shape, and Albedo of 2003 EL61, a Rapidly Rotating, Pluto-sized Object in the Kuiper Belt. ApJ 639, 1238–1251.

Roush, T. L., Dec. 2001. Physical state of ices in the outer solar system. JGR 106, 33315–33324.

Smith, B. A., Soderblom, L. A., Banfield, D., Barnet, C., Beebe, R. F., Bazilevskii, A. T., Bollinger, K., Boyce, J. M., Briggs, G. A., Brahic, A., Dec. 1989. Voyager 2 at Neptune - Imaging science results. Science 246, 1422–1449.

Smith, B. A., Soderblom, L. A., Beebe, R., Bliss, D., Brown, R. H., Collins, S. A., Boyce, J. M., Briggs, G. A., Brahic, A., Cuzzi, J. N., Morrison, D.,

Jul. 1986. Voyager 2 in the Uranian system - Imaging science results. Science 233, 43–64.

Spahn, F., Albers, N., Hörning, M., Kempf, S., Krivov, A. V., Makuch, M., Schmidt, J., Seiß, M., Miodrag Sremčević, Aug. 2006. E ring dust sources: Implications from Cassini's dust measurements. Planet. Space Sci. 54, 1024–1032.

Trujillo, C. A., Brown, M. E., Barkume, K. M., Schaller, E. L., Rabinowitz, D. L., Feb. 2007. The Surface of 2003 EL_{61} in the Near-Infrared. ApJ 655, 1172–1178.

Waite, J. H., Combi, M. R., Ip, W.-H., Cravens, T. E., McNutt, R. L., Kasprzak, W., Yelle, R., Luhmann, J., Niemann, H., Gell, D., Magee, B., Fletcher, G., Lunine, J., Tseng, W.-L., Mar. 2006. Cassini Ion and Neutral Mass Spectrometer: Enceladus Plume Composition and Structure. Science 311, 1419–1422.

Object	V_{net} (km/s)	$n_{\mathrm{imp}}/$ $n_{\mathrm{imp}}^{\infty}$	Annealing Time (kyr)	% Crystalline w/UV Amor.	Annealing effective with: UV	GCR	10x
Mimas	25.3	12.7	4.39	97.2	Yes	Yes	Yes
Enceladus	22.5	10.7	7.90	95.0	Yes	Yes	Yes
Tethys	20.5	9.21	12.9	92.1	Yes	Yes	Yes
Dione	18.3	7.69	22.9	86.8	Yes	Yes	Yes
Rhea	15.9	6.03	49.0	75.4	Yes	Yes	Yes
Hyperion	9.73	3.00	567	20.9	Yes	Yes	Yes
Iapetus	7.55	1.88	2290	6.16	No	Yes	Yes
Phoebe	5.15	1.26	13500	1.10	No	Maybe	No
Miranda	12.1	6.88	121	45.3	Yes	Yes	Yes
Ariel	10.5	5.24	264	27.5	Yes	Yes	Yes
Umbriel	9.10	4.19	557	15.2	Maybe	Yes	Yes
Titania	7.71	3.05	1390	6.72	No	Yes	Yes
Oberon	6.89	2.57	2460	3.91	No	Yes	Yes
Proteus	13.6	12.4	42.2	54.2	Yes	Yes	Yes
Triton	9.42	5.41	364	12.1	Maybe	Yes	Yes
Nereid	3.12	1.34	65200	0.0767	No	No	No

Table 1
Micrometeorite annealing results for the saturnian, uranian, and neptunian satellite systems. 'GCR' discounts all amorphization but by galactic cosmic rays, and '10x' scales the IDP flux by ten while assuming UV amorphization.

Object	Semimajor axis (AU)	Surface Temp. (K)	V_{net} (km/s)	Needed $F_{\mathrm{imp}}^{\infty}$ (kg s^{-1}m^{-2}):	
				UV	GCR
Orcus	39.2	45	2.48	1.9e-17	5.1e-19
Charon	39.5	40	2.61	1.9e-17	5.0e-19
Pluto	39.5	40	3.25	1.6e-17	4.4e-19
Haumea	43.1	40	2.79	1.8e-17	4.9e-19
Quaoar	43.6	45	2.64	1.8e-17	4.9e-19
Makemake	45.8	35	2.69	1.9e-17	5.1e-19
Eris	67.7	40	2.85	1.8e-17	4.9e-19
Sedna	526	35	1.02	1.4e-16	3.6e-18

Table 2

Micrometeorite annealing results for selected Kuiper Belt objects. $F_{\mathrm{imp}}^{\infty}$ is the IDP mass flux required to produce an annealed fraction of 20%, and assumes an amorphization time of 40 kyr for UV and 1.5 Myr for GCR.
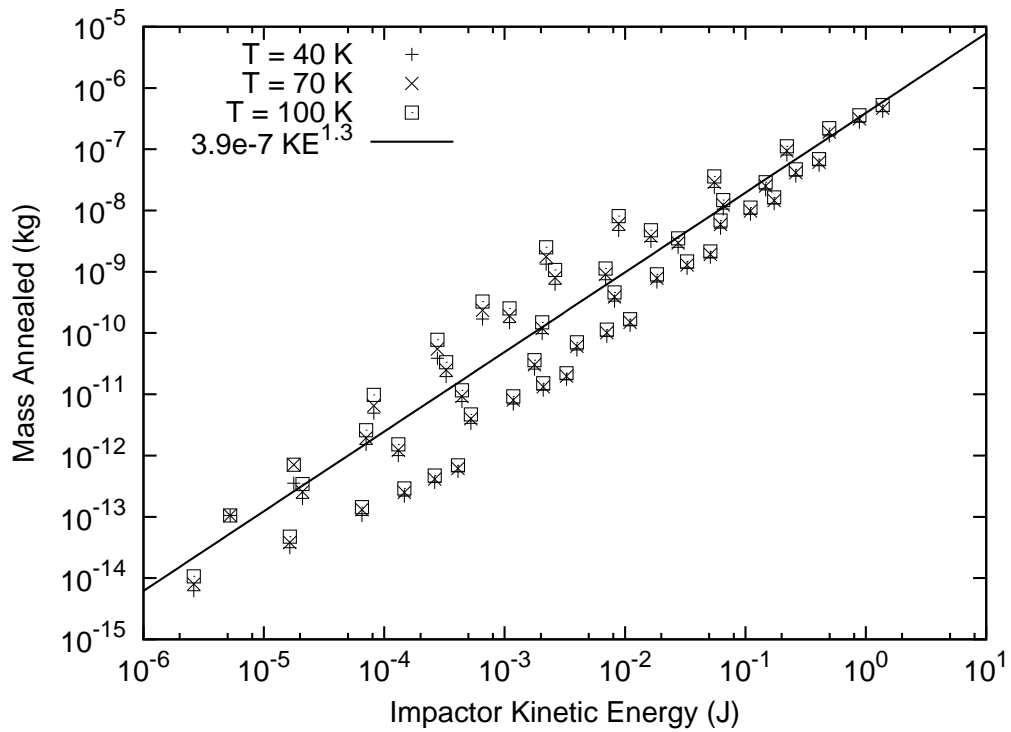
Fig. 1. Mass of ice annealed as a function of impactor kinetic energy and surface temperature. The symbols are data points produced by the diffusion simulation, and the line is a regression fit.
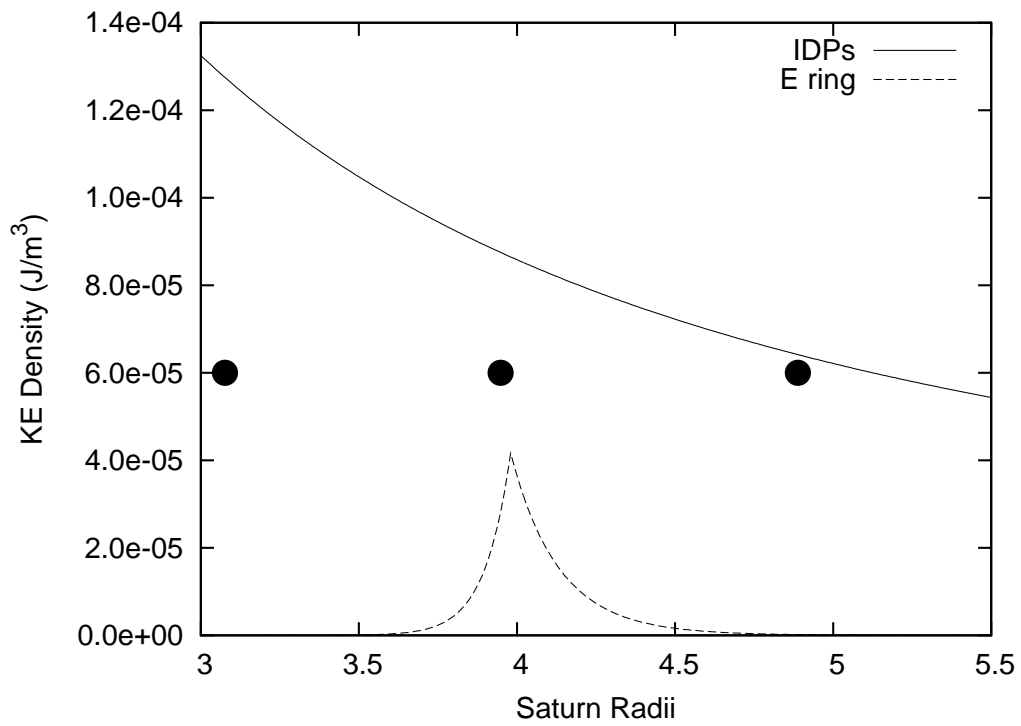
Fig. 2. Sum of kinetic energy per unit volume around Saturn for IDP and E-Ring particles from the model of Spahn et al. (2006). The three circles represent the orbits of Mimas, Enceladus, and Tethys.